

FAR-INFRARED LUMINOUS SUPERNOVA REMNANT KES 17

HO-GYU LEE¹, DAE-SIK MOON¹, BON-CHUL KOO², TAKASHI ONAKA³, WOONG-SEOB JEONG⁴, JONG-HO SHINN⁴, AND
 ITSUKI SAKON³

Submitted: November 7, 2018

ABSTRACT

We present the results of infrared (IR; 2.5–160 μm) observations of the supernova remnant (SNR) Kes 17 based on the data obtained with the *AKARI* and *Spitzer* satellites. We first detect bright continuum emission of its western shell in the mid- and far-IR wavebands together with its near-IR molecular line emission. We also detect hidden mid-IR emission of its southern shell after subtraction of the background emission in this region. The far-IR luminosity of the western shell is $\sim 8100 L_{\odot}$, which makes Kes 17 one of the few SNRs of significant far-IR emission. The fittings of the spectral energy distribution indicate the existence of two dust components: ~ 79 K (hot) and ~ 27 K (cold) corresponding to the dust mass of $\sim 6.2 \times 10^{-4} M_{\odot}$ and $\sim 6.7 M_{\odot}$, respectively. We suggest that the hot component represents the dust emission of the material swept up by the SNR to its western and southern boundaries, compatible with the distribution of radio continuum emission overlapping the mid-IR emission in the western and southern shells. The existence of hot ($\sim 2,000$ K), shocked dense molecular gas revealed by the near-IR molecular line emission in the western shell, on the other hand, suggests that the cold dust component represents the dust emission related to the interaction between the SNR and nearby molecular gas. The excitation conditions of the molecular gas appear to be consistent with those from shocked, clumpy admixture gas of different temperatures. We discuss three possibilities for the origin of the bright far-IR emission of the cold dust in the western shell: the emission of dust in the inter-clump medium of shocked molecular clouds, the emission of dust in evaporating flows of molecular clouds engulfed by hot gas, and the emission of dust of nearby molecular clouds illuminated by radiative shocks.

Subject headings: ISM: clouds — ISM: individual (Kes 17, G304.6+0.1) — infrared: ISM — shock waves — supernova remnants

1. INTRODUCTION

The broad-band infrared (IR) observations are well suited for the study of the evolution of SNRs. Besides the general advantage of suffering less extinction effects, there are diverse important phenomena related to supernova remnants (SNRs) which are bright in the IR wavebands. In the near- and mid-IR regimes, for example, one can study the distributions of dense ejecta from core-collapse supernova explosions (e.g., Koo et al. 2007; Moon et al. 2009), circumstellar material produced by mass loss of the progenitors (e.g., Dwek et al. 2008; Lee et al. 2009a,b), shock interactions between SNRs and nearby molecular clouds (e.g., Burton et al. 1988; Oliva et al. 1990; Reach et al. 2005; Neufeld et al. 2007; Hewitt et al. 2009; Shinn et al. 2009), and hot dust synthesized in ejecta (e.g., Arendt et al. 1999; Rho et al. 2008), along with the emission from the central compact objects (e.g., Moon et al. 2004; Kaplan et al. 2006; Wang et al. 2006).

The far-IR observations of SNRs, on the other hand,

are relatively rare but very efficient to investigate cold dust which often contributes to a significant portion of the total mass of the dust in SNRs. First, it is studied that the swept-up dust in SNRs is responsible for the most of cooling of SNRs and plays a critical role in the evolutions of SNRs in dense medium (Dwek et al. 1987). Secondly, the far-IR observations of SNRs appear to provide better means of studying the dust formed during the process of supernova explosion (e.g., Sibthorpe et al. 2010; Barlow et al. 2010). Finally, if an SNR is interacting with a nearby molecular cloud, its far-IR emission is expected to be significantly enhanced by the swept-up, inter-clump medium in the cloud or by the evaporation of dense clumps (e.g., Draine 1981; Dwek 1981), although the reality of these processes is yet to be confirmed observationally.

Kes 17, known as G304.6+0.1, is such an object in which broad-band IR observations can play an important role in our understanding of SNRs. Until recently this SNR has only been studied in radio continuum and OH line observations (Shaver & Goss 1970; Milne & Dickel 1975; Whiteoak & Green 1996; Frail et al. 1996), revealing broken radio shell structures in the west and south. The recent *Spitzer* observations, however, detected very bright IR emission in the 3–8 μm range (Lee 2005; Reach et al. 2006), which makes it in fact one of the brightest SNRs in the wavelength range. The follow-up spectroscopic observations in the 5–30 μm range also detected many strong H₂ emission lines (Hewitt et al. 2009). Very recently, the XMM-Newton X-ray obser-

¹ Department of Astronomy and Astrophysics, University of Toronto, Toronto, ON M5S 3H4, Canada; hglee@astro.utoronto.ca, moon@astro.utoronto.ca

² Department of Physics and Astronomy, Seoul National University, Seoul 151-742, Korea; koo@astrohi.snu.ac.kr

³ Department of Astronomy, Graduate School of Science, The University of Tokyo, Bunkyo-ku, Tokyo 113-0033, Japan; onaka@astron.s.u-tokyo.ac.jp, isakon@astron.s.u-tokyo.ac.jp

⁴ Korea Astronomy and Space Science Institute, 776, Daedeok-daero, Yuseong-gu, Daejeon 305-348, Korea; jeongws@kasi.re.kr, jhshinn@kasi.re.kr

vations detected centrally filled thermal X-ray emission inside the non-thermal radio shell, listing it as a member of the class of mixed-morphology SNRs (Combi et al. 2010). All these indicate that Kes 17 is interacting with nearby molecular gas and that more IR observations are needed to better understand its nature. In this paper, we present extensive broad-band IR observations of Kes 17 using the *AKARI* satellite, together with new analyses of archival *Spitzer* and radio continuum data. For the distance to Kes 17, only a lower limit of 8 kpc, corrected for the distance between the Sun and the Galactic center of 8.5 kpc, is known from the observations of H I line (Caswell et al. 1975). We adopt a distance of $8 d_8$ kpc where d_8 is a scaling factor in this paper.

2. OBSERVATIONS AND DATA

2.1. *AKARI* observations

The *AKARI* imaging observations of Kes 17 were carried out covering the mid-IR (13–27 μm) and far-IR (50–180 μm) bands on 2007 February 5 and 6, respectively. The journal of the *AKARI* observations is given in Table 1. The mid-IR observations were made by the Infrared Camera (IRC) equipped with an Si:As detector array of 256×256 pixels which produced two images of $10' \times 10'$ centered on 15 μm (IRC L15) and 24 μm (IRC L24) (Onaka et al. 2007). The total on-source integration time was 196 s for both images. The basic calibration and data handling such as dark subtraction, linearity fitting, distortion correction, flat fielding, image combination and astrometric measurement were performed by IRC Imaging Data Reduction Pipeline version 20110225⁵. The far-IR observations, on the other hand, were made by the Far-Infrared Surveyor (FIS) in two round-trip scans in the cross-scan shift mode (Kawada et al. 2007). The scan speed and shift length were $15'' \text{ s}^{-1}$ and $240''$, respectively, and the resulting imaging size was $40' \times 12'$ elongated in the scan direction. All the four FIS band (N60, Wide-S, Wide-L, and N160; see Table 2 for the details of the bands) images were obtained simultaneously in a single observing run using Ge:Ga (20×2 pixels for N60; 20×3 pixels for Wide-S) and stressed Ge:Ga (15×3 pixels for Wide-L; 15×2 pixels for N160) detector arrays. The initial calibration and data handling such as glitch detection, dark subtraction, flat fielding and flux calibration were performed by FIS Slow-Scan Toolkit version 20070914⁶, followed by advanced image construction based on the refined sampling mechanism. A summary of imaging bands used in this paper, including six *AKARI* bands (IRC L15, IRC L24, FIS N60, FIS Wide-S, FIS Wide-L, and FIS N160) and three *Spitzer* bands (IRAC 4.5, IRAC 8, and MIPS 24), is given in Table 2.

The *AKARI* spectroscopic observations were carried out in the near-IR slit mode on 2008 August 8 and 2009 February 4–6 (Table 1), which produced grism spectra of $R \simeq 120$ spectral resolving power in the 2.5–5.0 μm wavelength range (Ohya et al. 2007). Spectra of the two bright peaks and the narrow filament in the western shell of Kes 17 previously identified in *Spitzer* IRAC images

(Lee 2005; Reach et al. 2006) were obtained. The slit positions and their coordinates are presented in Figure 1 and in Table 3, respectively. The $5'' \times 0''.8$ slit was used for the target observations, whereas background spectra, which were subtracted from the target spectra later, were simultaneously obtained using the $3'' \times 1''$ slit positioned $1'$ apart from the targets. The data calibration and handling were performed by IRC Spectroscopy Toolkit version 20081015⁷.

2.2. *Spitzer* Infrared and ATCA Radio Continuum Data

Previous *Spitzer* studies detected bright IR emission of Kes 17 in the IRAC bands between 3.6 and 8.0 μm bands (Lee 2005; Reach et al. 2006). We used the *Spitzer* IRAC images of 4.5 and 8.0 μm bands in this paper. We analyzed the *Spitzer* archival data of MIPS 24 μm band⁸ (Carey et al. 2009) to make an image of $\sim 1^\circ$ size of Kes 17. For the 24 μm band image, we used the *Spitzer* data in this paper, unless explicitly mentioned otherwise. In addition, we obtained the *Spitzer* IRS 8–38 μm and MIPS SED 52–97 μm spectra available from the *Spitzer* data archive⁹ to estimate contributions of line emission in the wavelength ranges.

We also obtained a high-resolution ($9''.17 \times 7''.36$) radio-continuum image of Kes 17 using the Australia Telescope Compact Array (ATCA) archival data provided by the Australia Telescope Online Archive¹⁰. We synthesized the radio-continuum image of Kes 17 from the 12-h exposure 1.4 GHz data obtained with the 1.5A array configuration on 2004 March 24 after calibration of the data with 1329–665.

3. INFRARED MORPHOLOGY OF KES 17

Figure 1 presents the *AKARI* and *Spitzer* near- to far-IR (4.5–160 μm) band images of Kes 17, together with the ATCA 20 cm radio-continuum image. The most conspicuous feature in the IR images is the bright emission of $\sim 5'$ in the western shell apparent in all of the IR bands. The emission appears to be clumpy and filamentary in the near- and mid-IR bands up to 24 μm , whereas it becomes unresolved in the longer (65–160 μm) wavelength images due to increasingly large beam sizes. This IR emission in the western shell partly overlaps that of the radio continuum emission. In addition to the bright western shell, there is relatively weak mid-IR (15 and 24 μm) emission in the southern shell overlapping the radio continuum emission in this region.

There exists noticeable background emission in the direction of Kes 17 in all the images longer than 4.5 μm (Figure 1), especially in the northeast. In order to identify the southern shell emission in the 15 and 24 μm images more clearly, we subtract the background emission from both the images as follows: first, given that both the 4.5 and 8 μm emission of Kes 17 is due to the same origin (i.e., emission from shocked H_2 ; see § 4 for the details) in the western shell, we obtain a linear correlation with a correlation coefficient $r \simeq 0.86$ between the 4.5 and 8 μm emission of the shell. Based on the correlation, we scale

⁵ <http://www.ir.isas.jaxa.jp/ASTRO-F/Observation/DataReduction/IRC/>

⁶ <http://www.ir.isas.jaxa.jp/ASTRO-F/Observation/DataReduction/FIS/>

⁷ <http://www.ir.isas.jaxa.jp/ASTRO-F/Observation/DataReduction/IRC/>

⁸ http://data.spitzer.caltech.edu/popular/mipsgal/20080718_enhanced/MIPS

⁹ <http://sha.ipac.caltech.edu/applications/Spitzer/SHA/>

¹⁰ <http://atoa.atnf.csiro.au>

the 4.5 μm emission to 8 μm and subtract the scaled emission from the observed 8 μm emission to create a background image at 8 μm . Next, we obtain a linear correlation of $r \simeq 0.89$ between the background 8 μm emission and the 24 μm emission outside the boundaries of Kes 17, and then scale the 8 μm emission to 24 μm using the correlation. We subtract the scaled emission from the observed emission at 24 μm , which finally gives the background-removed 24 μm image of Kes 17 (Figure 2). The peak surface brightnesses of the western shell after the background subtraction are 6.1 ± 1.5 and 6.4 ± 1.5 MJy sr^{-1} for 15 and 24 μm bands, respectively. We apply the same method to obtain the background-removed *AKARI* 15 and 24 μm images. In all these processes, we convolved the images of different beam sizes with that of the 24 μm images. In Figure 2 we can now easily identify the existence of the southern shell at 15 and 24 μm which overlaps that of the radio continuum. For far-IR images of 65, 90, 140, and 160 μm , we estimate the background emission by taking the median value in the region between 4' and 6' radius from the center of Kes 17. After background subtraction, the peak surface brightnesses of the western shell are 108 ± 24 , 135 ± 45 , 173 ± 84 , and 117 ± 55 MJy sr^{-1} for 65, 90, 140 and 160 μm bands, respectively.

Table 4 presents the measured (or upper limits) IR fluxes of the western and southern shells between 15 and 160 μm , together with the estimation of contributions of line emission in the bands. The errors in the flux measurements are mainly caused by the uncertainties in the background measurements and also by those associated with the calibrations of the *AKARI* and *Spitzer* observations. We estimate the line contributions to the observed fluxes of the 15 and 24 μm bands using the *Spitzer* IRS 8–38 μm spectra. We construct the IRS spectra by subtracting the background obtained outside the shell structure and integrate them over the bandpass. The estimated line contributions are 75 ± 21 (15 μm) and 38 ± 10 % (24 μm for both *AKARI* and *Spitzer*), respectively. The line emission in these bands is dominated by H_2 and ionic lines. We also estimate the contribution of line emission of the 60 and 90 μm bands to be 16 ± 8 and 3 ± 2 %, respectively, using *Spitzer* MIPS SED 52–97 μm spectra. The line contributions in these bands are mostly due to [O I] at 63 μm . For the 140 and 160 μm bands, we expect the line contributions to be less than 5 % by scaling the flux of the [O I] 63 μm line that we obtain above to those of [O I] 145 μm and [C II] 153 μm lines in a shocked region (Hollenbach & McKee 1989; Allen et al. 2008). Figure 3 shows the flux distribution of the western shell excluding the line contributions.

The IR synchrotron flux expected from an extrapolation of the radio fluxes applying synchrotron power-law index of -0.54 (Shaver & Goss 1970) is less than a few percents of the measured IR values, supporting that the observed continuum is dominated by dust emission. In order to calculate temperatures of the dusts responsible for the mid- and far-IR emission of Kes 17, we perform the spectral energy distribution (SED) fits of the flux distribution (Figure 3) with two modified blackbody components. For the emissivity of the dusts in the SED fits, we adopt a mixture of carbonaceous and silicate interstellar grains (Draine 2003). As a result, we obtain acceptable fit (reduced chi-square < 2) with dust temperature com-

ponents of 79 ± 6 K and 27 ± 3 K (Figure 3). The mass of the hot (79 K) dust is $(6.2 \pm 4.6) \times 10^{-4} d_8^2 M_\odot$ and that of the cold (27 K) dust is $6.7 \pm 4.0 d_8^2 M_\odot$. The luminosities of the dust emission are $(9.5 \pm 6.1) \times 10^2 d_8^2 L_\odot$ and $(8.1 \pm 5.0) \times 10^3 d_8^2 L_\odot$ for the hot and cold components, respectively. It is worthwhile to note that the hot dust temperature could have been overestimated if there is any contribution from stochastically heated small grains to the 15 and 24 μm continuum fluxes (Dwek 1986).

4. NEAR-INFRARED SPECTROSCOPY AND BRIGHT H_2 LINES

Figure 4 shows near-IR (2.5–5.0 μm) *AKARI* spectra of five points (A, B1, B2, C1, C2 in Figure 1) in the western shell of Kes 17 obtained after subtraction of the background spectrum. (See Table 4 for their coordinates.) We detect several H_2 lines in the spectra including the pure rotational transitions of 0-0 S(9–14) and ro-vibrational transitions of 1-0 O(3, 5, 6). Table 5 lists the observed intensities of the line emission.

Figure 5 presents the excitation diagram of the pure rotational and ro-vibrational H_2 lines of B2 between the upper energy level of 6,000 K and 20,000 K. For this we correct the extinction effect using the H column density of $3.6 \times 10^{22} \text{ cm}^{-2}$ estimated in previous X-ray observations of Kes 17 and the Galactic extinction curve (Hewitt et al. 2009; Draine 2003). The linear correlation between the upper energy level and the upper column density represented by a straight line in Figure 5 indicates the level population of the local thermodynamic equilibrium at the excitation temperature of 2200 ± 400 K. The spectra of other positions, which have smaller number of detected lines, show similar excitation temperatures to that of B2.

5. DISCUSSIONS

5.1. Origin of Bright Infrared Emission of Kes 17

The IR emission of Kes 17 shows the existence of both the western and southern shell structures. The former is visible in all the IR bands, while the latter is visible only in the mid-IR bands of 15 and 24 μm . The near-IR emission of the western shell is dominated by H_2 line emission (Figure 4), which suggests that Kes 17 is interacting with molecular gas in this region, consistent with the results of previous observations (e.g., Hewitt et al. 2009). The distribution of the mid-IR emission overlaps that of the radio continuum emission in the western and southern shells (Figure 2), supporting the interpretation that it represents swept-up dust at the boundary of the SNR. On the other hand, the far-IR emission is similar to the near-IR emission with only the western shell being readily identifiable. The coexistence of the far-IR emission from the cold dust and the near-IR line emission from shocked molecular gas in the western shell suggests that the bright far-IR emission of Kes 17 in this region is also related to the interaction of the source with a nearby molecular cloud.

The far-IR luminosity of Kes 17 ($\sim 8100 d_8^2 L_\odot$; § 3) makes it one of the most luminous SNRs in the far-IR wavebands and the second (after Cassiopeia A) Galactic SNR detected up to 160 μm in the IR wavebands (Sibthorpe et al. 2010). For comparison, only eight SNRs were detected by IRAS at 100 μm with far-IR luminosity larger than Kes 17 (Saken et al. 1992),

five of them interacting with molecular clouds (e.g., Koo & Moon 1997; Reach et al. 1999; Keohane et al. 2007; Hewitt et al. 2009). Our observations also strongly suggest that the far-IR emission of Kes 17 is originated from the dust in a molecular cloud interacting with the SNR. However, molecular shocks producing strong H_2 lines in a dense molecular cloud cannot directly generate bright far-IR dust continuum emission. This is because, in the non-dissociative molecular shock with shock speeds of $< 50 \text{ km s}^{-1}$, the gas temperature does not rise above a few thousand degrees (Draine 1981). This is inadequate to heat the dust grains sufficiently high enough to emit bright far-IR continuum emission. Instead, if a molecular cloud is clumpy, composed of clumps and inter-clump medium, then the far-IR emission may be produced by faster shocks propagating in the inter-clump medium of lower densities. Even though the density of inter-clump medium is lower than that of the H_2 emitting clumps, it can still be high enough to contain large amount of dusts and reduce shock speeds significantly. In the following we consider these possibilities.

When SNR shocks propagate into a clumpy molecular cloud, hot gas in swept-up inter-clump medium behind shock front collisionally heats dusts to produce the IR emission. The estimated dust mass of the western shell of Kes 17 is $6.7 \pm 4.0 d_8^2 M_\odot$. If the cloud initially occupies the entire western region with normal dust-to-gas ratio of 1 %, the pre-shock inter-clump density is $40 \pm 20 d_8^{-1} \text{ cm}^{-3}$. Assuming that Kes 17 is in a Sedov phase with radius of $\sim 7 d_8 \text{ pc}$, the shock velocity in the inter-clump medium is $v_{ic} \simeq 200 E_{51}^{0.5} (n_{ic}/40 \text{ cm}^{-3})^{-0.5} d_8^{-1.5} \text{ km s}^{-1}$, where E_{51} is the SN explosion energy in the unit of 10^{51} erg and n_{ic} is the density of the inter-clump medium. In this swept-up inter-clump gas, the IR surface brightness of the dust by strong shocks is (Draine 1981)

$$I_\nu \simeq 90 \left(\frac{n_{ic}}{40 \text{ cm}^{-3}} \right) \left(\frac{v_{ic}}{200 \text{ km s}^{-1}} \right)^3 \left(\frac{\lambda}{90 \mu\text{m}} \right) \text{ MJy sr}^{-1}$$

around $90 \mu\text{m}$, which, for the obtained inter-clump density and velocity of $\sim 40 \text{ cm}^{-3}$ and $\sim 200 \text{ km s}^{-1}$, gives comparable surface brightness to the observed value. Note that the calculation by Draine (1981) expects the peak of dust emission power (λf_λ) at the mid-IR wavelength ($\sim 30 \mu\text{m}$), while our observations indicate a somewhat flat λf_λ peak around the 65–90 μm bands. This is suggestive that there may be a significantly increased amount of large dusts contributing effectively in the far-IR regime if the shocked inter-clump medium is responsible for the observed emission of Kes 17.

Alternatively, the bright far-IR emission of Kes 17 may be the emission of dusts injected from an evaporating cloud (Dwek 1981). If so, the expected IR luminosity of an evaporating cloud in the hot gas of an SNR is (Dwek 1981)

$$L_{IR} \simeq 200 n_h^2 \left(\frac{R_c}{1 \text{ pc}} \right)^3 \left(\frac{T_h}{10^7 \text{ K}} \right)^{1.5} L_\odot$$

where R_c is the radius of the cloud and n_h and T_h are the density and temperature of the hot gas, respectively. The X-ray emitting gas was recently detected inside the radio shell of Kes 17 (Combi et al. 2010), suggesting that the

evaporation should occur at the surface of an IR emitting cloud where it is in contact with the hot interior gas. The temperature and density of the hot X-ray gas are $\sim 10^7 \text{ K}$ and $\sim 1 \text{ cm}^{-3}$, respectively (Combi et al. 2010). We expect the IR luminosity of an evaporating cloud to be $\sim 2,000 d_8^3 L_\odot$ using the cloud radius of $3 d_8 \text{ pc}$ ($\sim 1.3'$) at $90 \mu\text{m}$ (Figure 1). This is somewhat smaller than the observed far-IR luminosity ($\sim 8000 L_\odot$, § 3) of Kes 17, indicating that the dust emission from an evaporating cloud may contribute only a small amount of the far-IR emission of Kes 17, although we cannot rule out the possibility completely given the various uncertainties involved in the measurements.

Another explanation of the bright far-IR emission of Kes 17 may be that the dusts in a pre-shock molecular cloud heated by strong radiation of the SNR shocks in a radiative phase emit the observed emission. The shocks propagating into a molecular cloud at the western shell of Kes 17 can easily become radiative for the pre-shock density of $\lesssim 100 \text{ cm}^{-3}$ if gas cooling is efficient. Taking a power-law temperature dependence of the cooling efficiencies ($\propto T^{-0.5}$; Kahn 1976), Cox et al. (1999) calculated a radiative shell forming at the radius $R_{sh} \simeq 7 E_{51}^{1/8} t_{10}^{3/4} \text{ pc}$ with a shell velocity $v_{sh} \simeq 200 E_{51}^{1/8} t_{10}^{1/4} \text{ km s}^{-1}$ for a pre-shock density $n_o \simeq 20 E_{51}^{3/8} t_{10}^{-7/4} \text{ cm}^{-3}$ and a radiative shell forming time $t_{10} = 10,000 \text{ yrs}$. This indicates that Kes 17 likely has a radiative shell, if the pre-shock density is $\gtrsim 20 \text{ cm}^{-3}$. Using the shell forming values and a cloud radius of $R_c = 3 d_8 \text{ pc}$, the luminosity of a radiative shock at the western shell of Kes 17 is expected to be (Hollenbach & McKee 1989)

$$L \simeq 2.6 \times 10^4 \left(\frac{R_c}{3 \text{ pc}} \right)^2 \left(\frac{n_o}{20 \text{ cm}^{-3}} \right) \left(\frac{v_s}{200 \text{ km s}^{-1}} \right)^3 L_\odot$$

which appears to be adequate to explain the observed luminosity of the western shell (§ 3). In this case, we expect the peak of the dust emission power to be at the far-IR ($\geq 60 \mu\text{m}$) region for the dusts of mixture of carbonaceous and silicate grains (Draine 2011), consistent with the results of this study. This can also explain the absence of the X-ray emission in the western shell of Kes 17 as the lack of X-ray emitting high temperature gas in the radiative phase (Combi et al. 2010).

5.2. Thermal Admixture Model of Molecular Shocks

Our near-IR (2.5–5.0 μm) spectra of the western shell of Kes 17 indicate the excitation temperature of $2200 \pm 400 \text{ K}$ for H_2 gas in this region (Figure 4). This is different from the previous results based on the *Spitzer* observations where a mixture of two components of H_2 gas of $\sim 300 \text{ K}$ and $\sim 1200 \text{ K}$ was proposed to explain the observed intensity distribution of H_2 lines of the western shell in the 5–28 μm range (Hewitt et al. 2009). The discrepancy in the excitation temperature suggests that the H_2 gas in the western shell is in a thermal admixture as found in other H_2 gas interacting with SNRs (Neufeld & Yuan 2008; Shinn et al. 2009, 2010).

Figure 6 shows the excitation diagram of H_2 lines detected in both the *Spitzer* and *AKARI* observations, covering the upper energy level of 1000–17,000 K. (Note that while the *Spitzer* results represent the levels of \lesssim

7,000 K, the *AKARI* results do the levels of higher temperatures.) We fit the observed excitation diagram with a thermal admixture model where the column density of H_2 gas is related to a power of its temperature of 100–4,000 K: $dN \sim T^{-b} dT$ (Shinn et al. 2009, 2010). The ortho-to-para ratio is fixed to be 3 in the fit. The best fit gives 3.0 ± 0.1 , $(1.5 \pm 0.2) \times 10^{21} \text{ cm}^{-2}$, and $(3.2 \pm 0.7) \times 10^5 \text{ cm}^{-3}$ for the power index, column density, and number density, respectively. The solid curve in Figure 6 represents the best-fit model to the observed data, where we can identify that the model prediction matches the observed values well. This column density is twice that of the two temperature model of the *Spitzer* observations, while the number density is between those obtained for the warm and hot components of the *Spitzer* results (Hewitt et al. 2009). The obtained power index of 3.0 ± 0.1 is comparable to what obtained from other sources (Shinn et al. 2009; Neufeld & Yuan 2009), and is not far from 3.8 obtained for bow shocks (Neufeld & Yuan 2008). If Kes 17 is indeed interacting with clumpy molecular gas (see § 5.1), it can be easy to develop a group of shocks around dense clumps with various shock velocities, which in turn naturally leads to an admixture of H_2 gas of different temperatures.

6. CONCLUSION

We show in this paper that Kes 17 is one of the most luminous SNRs in the IR wavebands, reaching the far-IR luminosity of $\sim 8100 L_\odot$. Its IR emission is concentrated on the western and southern shell structures. The western shell is bright in the mid- and far-IR continuum and the near-IR H_2 line emission, whereas the southern shell is visible only in the mid-IR continuum emission. The far-IR continuum and near-IR H_2 line emission of the western shell is related to its interaction with nearby molecular gas. It is apparent that there exists dense shocked molecular gas, excited to $\sim 2,000$ K, in this region that produces the observed H_2 line emission. If the molecular gas is clumpy, the observed far-IR emission can be produced by the dust associated with inter-clump molecular gas of lower densities. The far-IR emission may originate from the dust emission of the swept-up inter-clump molecular gas, the dust emission from an

evaporating cloud, or the dust emission exposed to strong radiative shocks. The mid-IR emission of Kes 17 is bright in both the western and southern shells and overlaps radio continuum emission which forms a partly-broken circular shell structure. This suggests that the mid-IR and radio continuum emission delineates the boundary of Kes 17 made by the swept-up material.

The SED distribution of the IR emission of Kes 17 indicates the existence of two dust components: hot (79 ± 6 K) component of $(6.2 \pm 4.6) \times 10^{-4} d_8^2 M_\odot$ and cold (27 ± 3 K) component of $6.7 \pm 4.0 d_8^2 M_\odot$. The former is responsible for most of the mid-IR continuum emission, while the latter is for the far-IR emission. The observed flux distribution of the H_2 lines, on the other hand, can be explained with a thermal admixture of the shocked molecular gas of different temperatures in the 100–4,000 K range. This thermal admixture of the shocked molecular gas may be a natural consequence of the interactions between Kes 17 and clumpy molecular gas in which various shock velocities can easily produce thermal admixture of the molecular gas. Overall, it appears that combined far-IR continuum and near-IR spectroscopic observations are very useful to studying SNRs interacting with molecular gas, as was the case for Kes 17 in this paper, providing information for both the gas and dust components associated with the shock interactions.

This work is based on observations with *AKARI*, a JAXA project with the participation of ESA. This work is based in part on observations made with the *Spitzer* Space Telescope, which is operated by the Jet Propulsion Laboratory, California Institute of Technology under a contract with NASA. The Australia Telescope Compact Array is part of the Australia Telescope which is funded by the Commonwealth of Australia for operation as a National Facility managed by CSIRO. We thank all the members of the *AKARI* project. We also thank an anonymous referee for constructive comments. H.-G.L. was supported by the Early Research Award Program (ERA07-03-270) to D.-S.M. from Ministry of Research and Innovation of the Ontario Provincial Government. D.-S.M. acknowledges the support by NSERC through Discovery program 327277. B.-C.K. was supported by the National Research Foundation of Korea (NRF) Grant (NRF-2010-616-C00020).

Facility: AKARI, Spitzer, ATCA

REFERENCES

- Allen, M. G., Groves, B. A., Dopita, M. A., Sutherland, R. S., & Kewley, L. J. 2008, *ApJS*, 178, 20
 Arendt, R. G., Dwek, E., & Moseley, S. H. 1999, *ApJ*, 521, 234
 Barlow, M. J. et al. 2010, *A&A*, 518, 138
 Burton, M. G., Brand, P. W. J. L., Geballe, T. R., & Webster, A. S. 1988, *MNRAS*, 235, 161
 Carey, S. J., et al. 2009, *PASP*, 121, 76
 Caswell, J. L., Murray, J. D., Roger, R. S., Cole, D. J., & Cooke, D. J. 1975, *A&A*, 45, 239
 Combi, J. A. et al. 2010, *A&A*, 523, 76
 Cox, D. P., Shelton, R. L., Maciejewski, W., Smith, R. K., Plewa, T., Pawl, A., Różyczka, M. 1999, *ApJ*, 524, 179
 Draine, B. T., 1981, *ApJ*, 245, 880
 Draine, B. T., 2003, *ARA&A*, 41, 241
 Draine, B. T., 2011, *Physics of the Interstellar and Intergalactic Medium*, (Princeton, NJ; Princeton University Press)
 Dwek, E., 1981, *ApJ*, 430, 433
 Dwek, E., 1986, *ApJ*, 302, 363
 Dwek, E., Petre, R., Szymkowiak, A., & Rice, W. L. 1987, *ApJ*, 320, L27
 Dwek, E., et al. 2008, *ApJ*, 676, 1029
 Fazio, G. G., et al. 2004, *ApJS*, 154, 10
 Frail, D. A., Goss, W. M., Reynoso, E. M., Giacani, E. B., Green, A. J., & Otrupcek, R. 1996, *AJ*, 111, 1651
 Hewitt, John W., Rho, J., Andersen, M., & Reach, W. T. 2009, *ApJ*, 694, 1266
 Hollenbach, D., & McKee, C. F. 1989, *ApJ*, 342, 306
 Kahn, F. D. 1976, *A&A*, 50, 145
 Kaplan, D. L., & Moon, D.-S. 2006, *ApJ*, 644, 1056
 Kawada, M., Baba, H., Barthel, P. D. et al. 2007, *PASJ*, 59, 389
 Keohane, J. W., Reach, W. T., Rho, J., & Jarrett, T. H. 2007, *ApJ*, 654, 938
 Koo, B.-C., & Moon, D.-S. 1997, *ApJ*, 485, 263
 Koo, B.-C., Moon, D.-S., Lee, H.-G., Lee, J.-J., & Matthews, K. 2007, *ApJ*, 657, 308
 Lee, H.-G. 2005, *JKAS*, 38, 385
 Lee, H.-G. Moon, D.-S., Koo, B.-C., Lee, J.-J., & Matthews, K. 2009, *ApJ*, 691, 1042

- Lee, H.-G. Koo, B.-C., Moon, D.-S., Sakon, I., Onaka, T., Jeong, W.-S., Kaneda, H., Nozawa, T., & Kozasa, T. 2009, *ApJ*, 706, 441
- Milne, D. K., & Dickel, J. R. 1975, *AuJPh*, 28, 209
- Moon, D.-S., Lee, J.-J., Eikenberry, S. S., Koo, B.-C., Chatterjee, S., Kaplan, D. L., Hester, J. J., Cordes, J. M., Gallant, Y. A., Koch-Miramond, L. 2004, *ApJ*, 610, 33
- Moon, D.-S., Koo, B.-C., Lee, H.-G., Matthews, K., Lee, J.-J., Pyo, T.-S., Seok, J. Y., & Hayashi, M. 2009, *ApJ*, 703, 81
- Neufeld, D. A., Hollenbach, D. J., Kaufman, M. J., Snell, R. L., Melnick, G. J., Bergin, E. A., & Sonnentrucker, P. 2007, *ApJ*, 664, 890
- Neufeld, D. A. & Yuan, Y. 2008, *ApJ*, 678, 974
- Neufeld, D. A. Nisini, B., Giannini, T., Melnick, G. J., Bergin, E. A., Yuan, Y., Maret, S., Tolls, V., Güsten, R., & Kaufman, M. J. 2009, *ApJ*, 706, 170
- Oliva, E., Moorwood, A. F. M., & Danziger, I. J. 1990, *A&A*, 240, 453
- Onaka, T., Matsuhara, H., Wada, T. et al. 2007, *PASJ*, 59, 401
- Ohyama, Y., Onaka, T., Matsuhara, H. et al. 2007, *PASJ*, 59, 411
- Reach, W. T., & Rho, J. 1999, *ApJ*, 511, 836
- Reach, W. T., Rho, J., & Jarrett, T. H. 2005, *ApJ*, 618, 297
- Reach, W. T., Rho, J., Tappe, A., Pannuti, T. G., Brogan, C. L., Churchwell, E. B., Meade, M. R., Babler, B., Indebetouw, R., & Whitney, B. A. 2006, *AJ*, 131, 1479
- Rho, J., Kozasa, T., Reach, W. T., Smith, J. D., Rudnick, L., DeLaney, T., Ennis, J. A., Gomez, H., & Tappe, A. 2008, *ApJ*, 673, 271
- Rieke et al. 2004, *ApJS*, 154, 25
- Saken, J. M., Fesen, R. A., & Shull, J. M. 1992, *ApJS*, 81, 715
- Shaver, P. A., & Goss, W. M. 1970, *AuJPA*, 14, 133S
- Shinn, J.-H., Koo, B.-C., Burton, M. G., Lee, H.-G., & Moon, D.-S. 2009, *ApJ*, 693, 1883
- Shinn, J.-H., Koo, B.-C., Burton, M. G., Lee, H.-G., & Moon, D.-S. 2010, *AdSpR*, 45, 445
- Sibthorpe, B., et al. 2010, *ApJ*, 719, 1553
- Wang, Z., Chakrabarty, D., & Kaplan, D. L. 2006, *Nature*, 440, 772
- Whiteoak, J. B. Z., & Green, A. J. 1996, *A&AS*, 118, 329

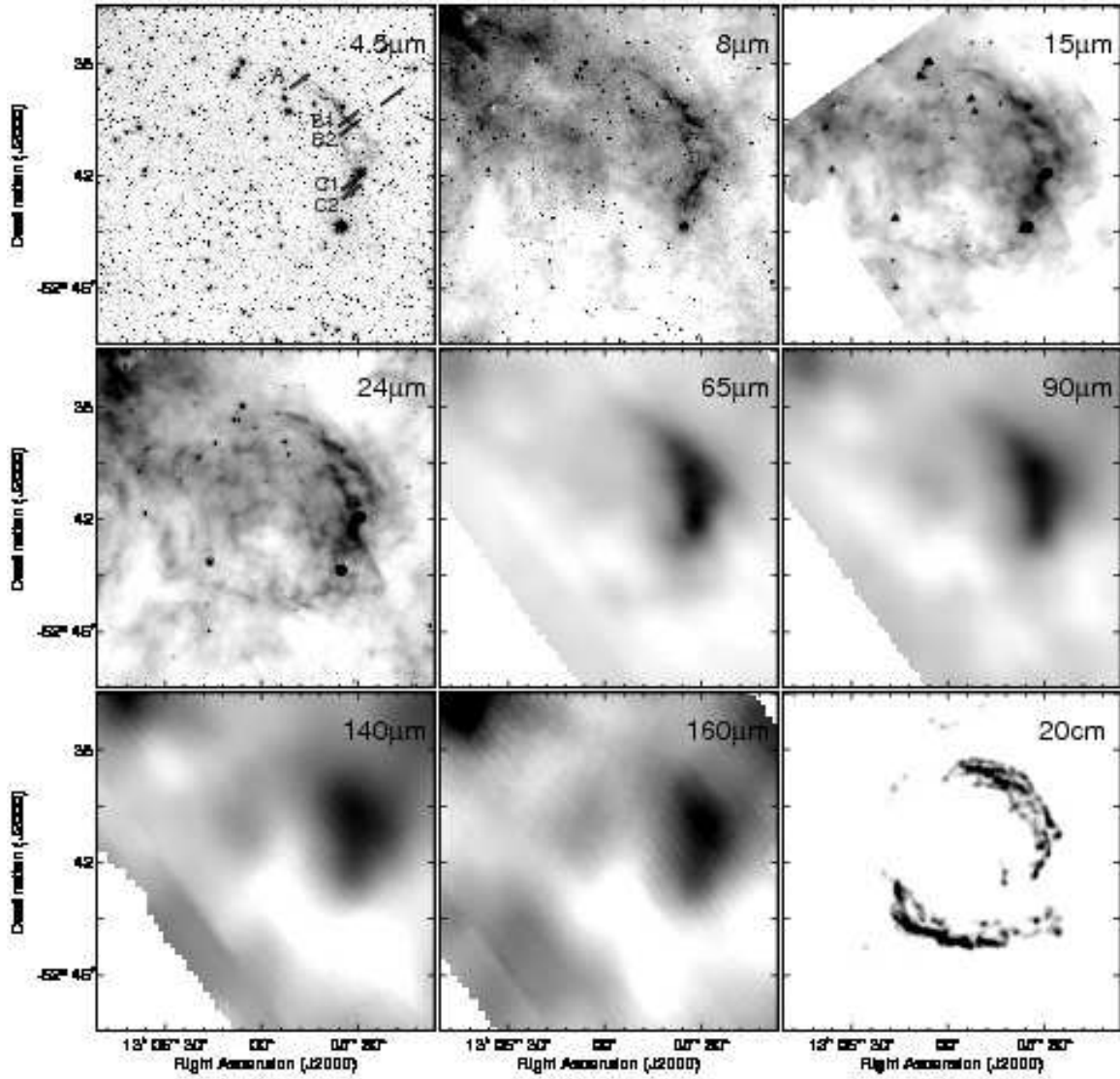


FIG. 1.— *AKARI* and *Spitzer* IR images of Kes 17, together with the *ATCA* 20 cm image. The wavelength of each imaging band is inserted at the upper-right corner of each panel. The 4.5, 8, and 24 μm images are from *Spitzer*, and the rest IR images are from *AKARI*. The slit positions of near-IR spectroscopic observations are shown in the 4.5 μm image (see Table 3 for the coordinates). The ranges of the gray scales are 1–10, 36–58, 43–56, 32–45, 160–290, 400–570, 1050–1300, and 700–850 MJy sr^{-1} for the 4.5, 8, 15, 24, 65, 90, 140, and 160 μm band images, respectively. The range of the gray scale of the radio continuum image is 0.001–0.01 Jy beam^{-1} .

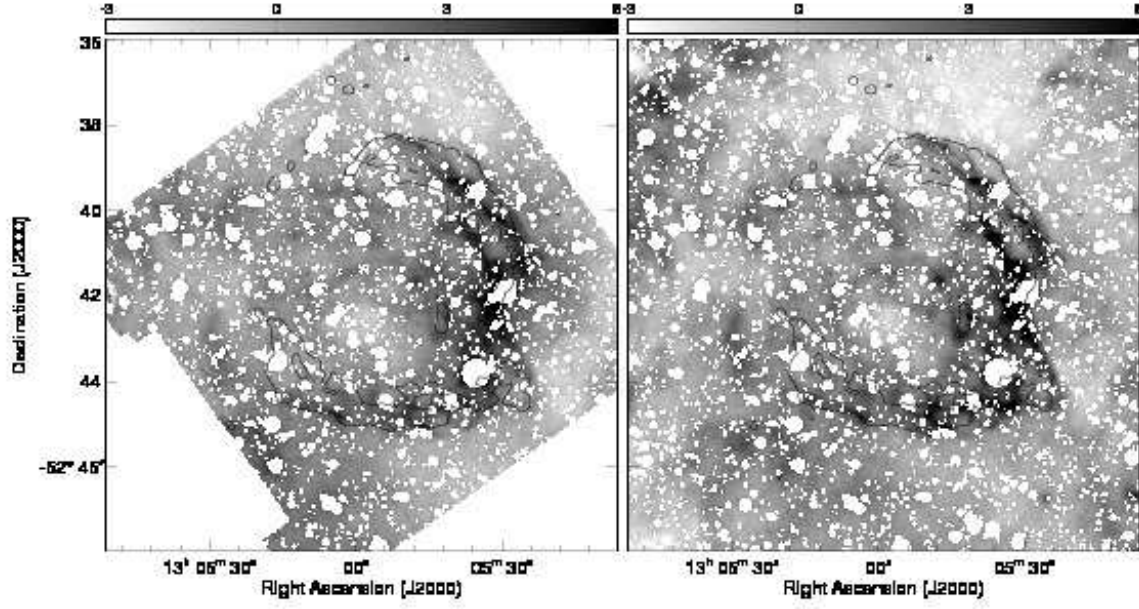


FIG. 2.— The background-removed 15 (left) and 24 μm (right) band images of Kes 17. The superposed contour is the 20 cm radio continuum emission boundary of $0.002 \text{ Jy beam}^{-1}$.

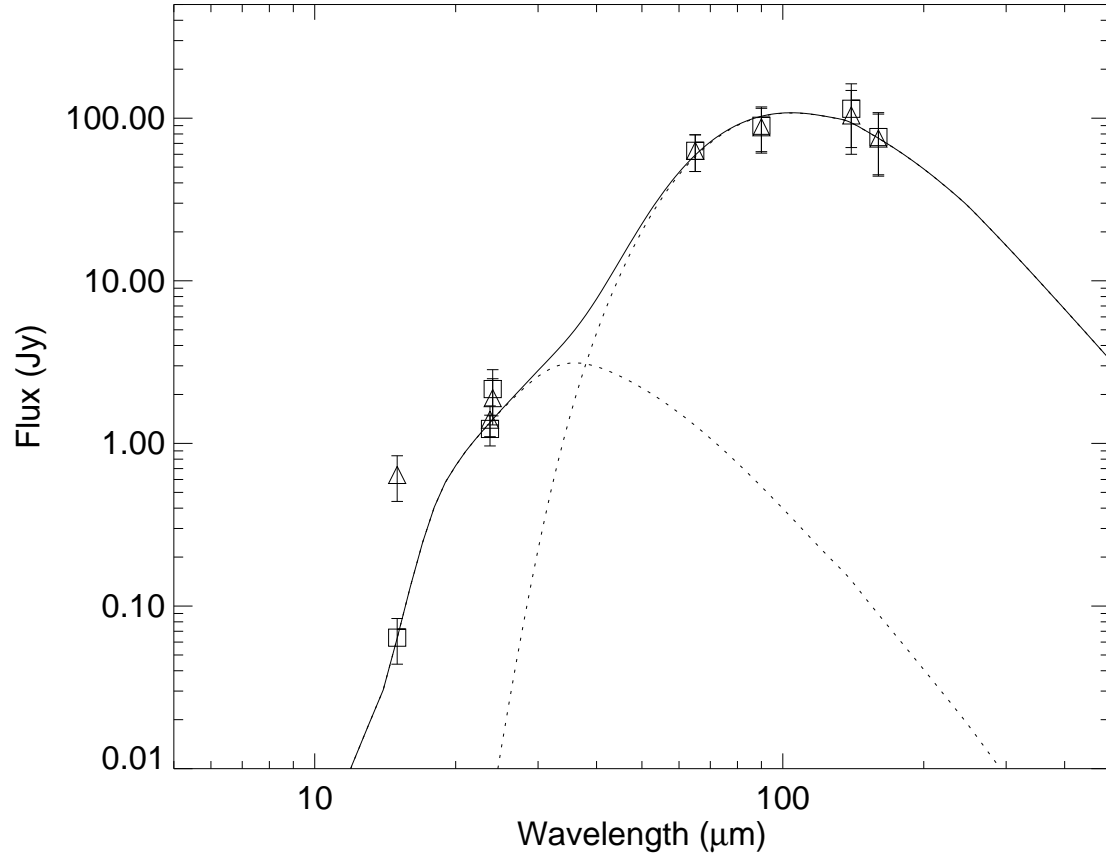


FIG. 3.— The IR fluxes of the western shell of Kes 17: the triangles are measured fluxes; the squares are color-corrected fluxes. We use the line-subtracted fluxes except 140 and 160 μm band fluxes where the line contributions are insignificant (see § 3). The two dotted curves show the modified blackbody radiation of 79 ± 6 K and 27 ± 3 K. The solid curve shows the combination of the two dotted curves.

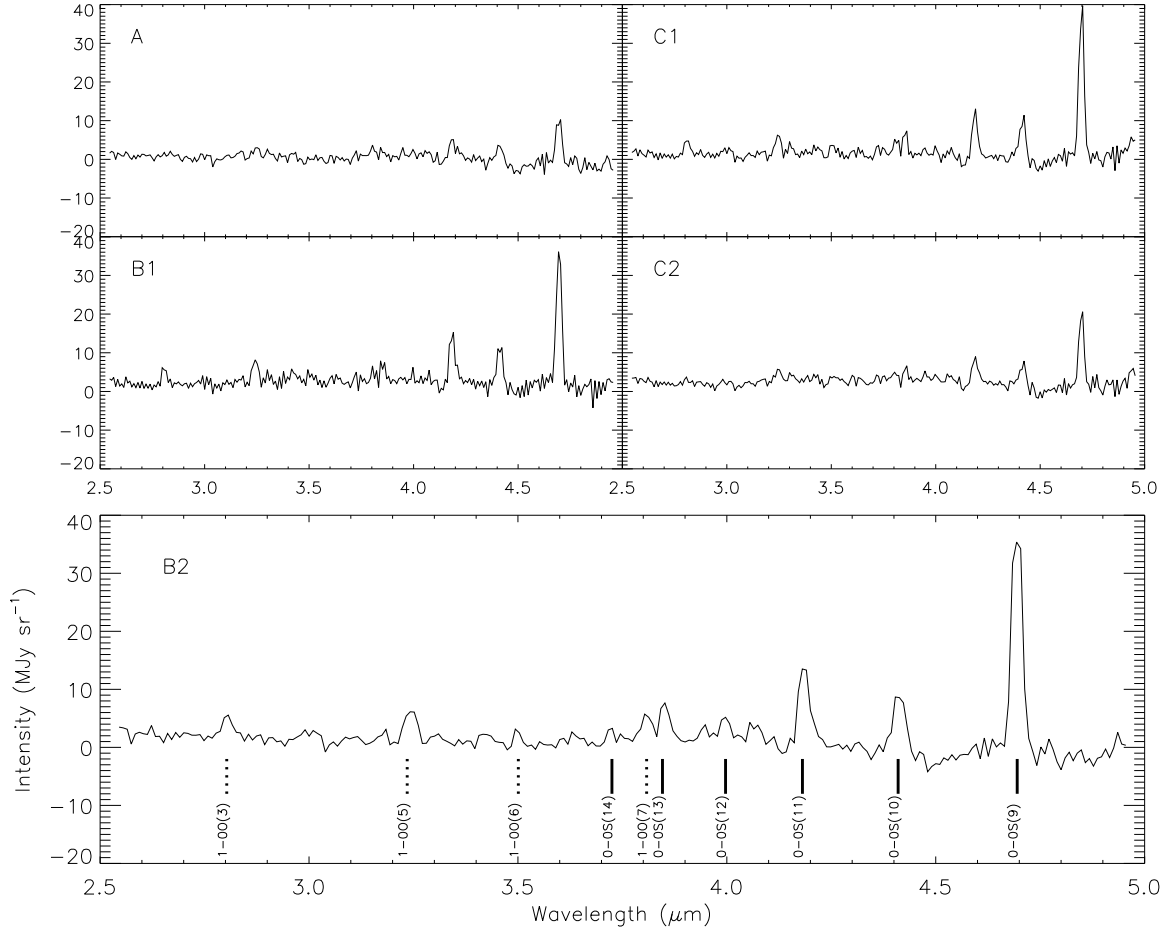


FIG. 4.— The *AKARI* near-IR spectra of Kes 17 from the five position (A, B1, B2, C1, C2) in the western shell. Their slit positions and coordinates are listed in Figure 1 and Table 3, respectively. We mark the identified pure rotational (solid) and ro-vibrational (dotted) H_2 lines in the bottom panel of the B2 position.

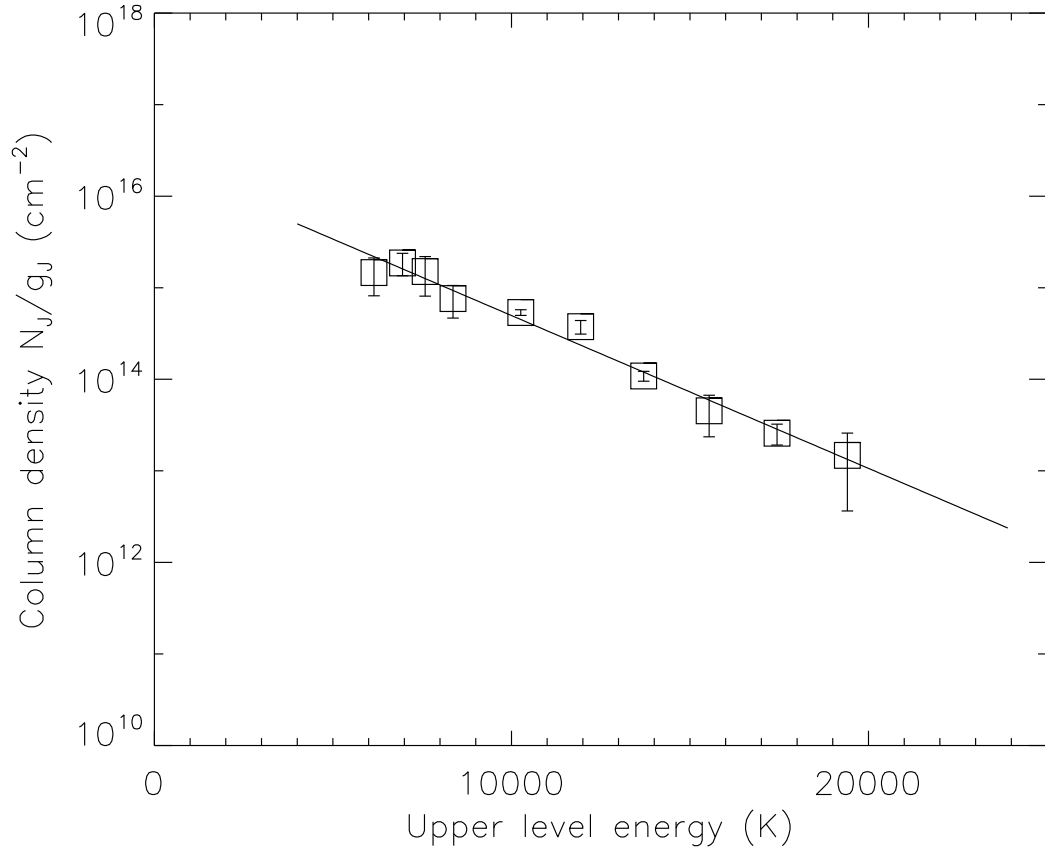


FIG. 5.— The *AKARI* H₂ line population diagram of the B2 position. The solid line shows the results of the linear fit of the observed fluxes with the excitation temperature of 2,200 K.

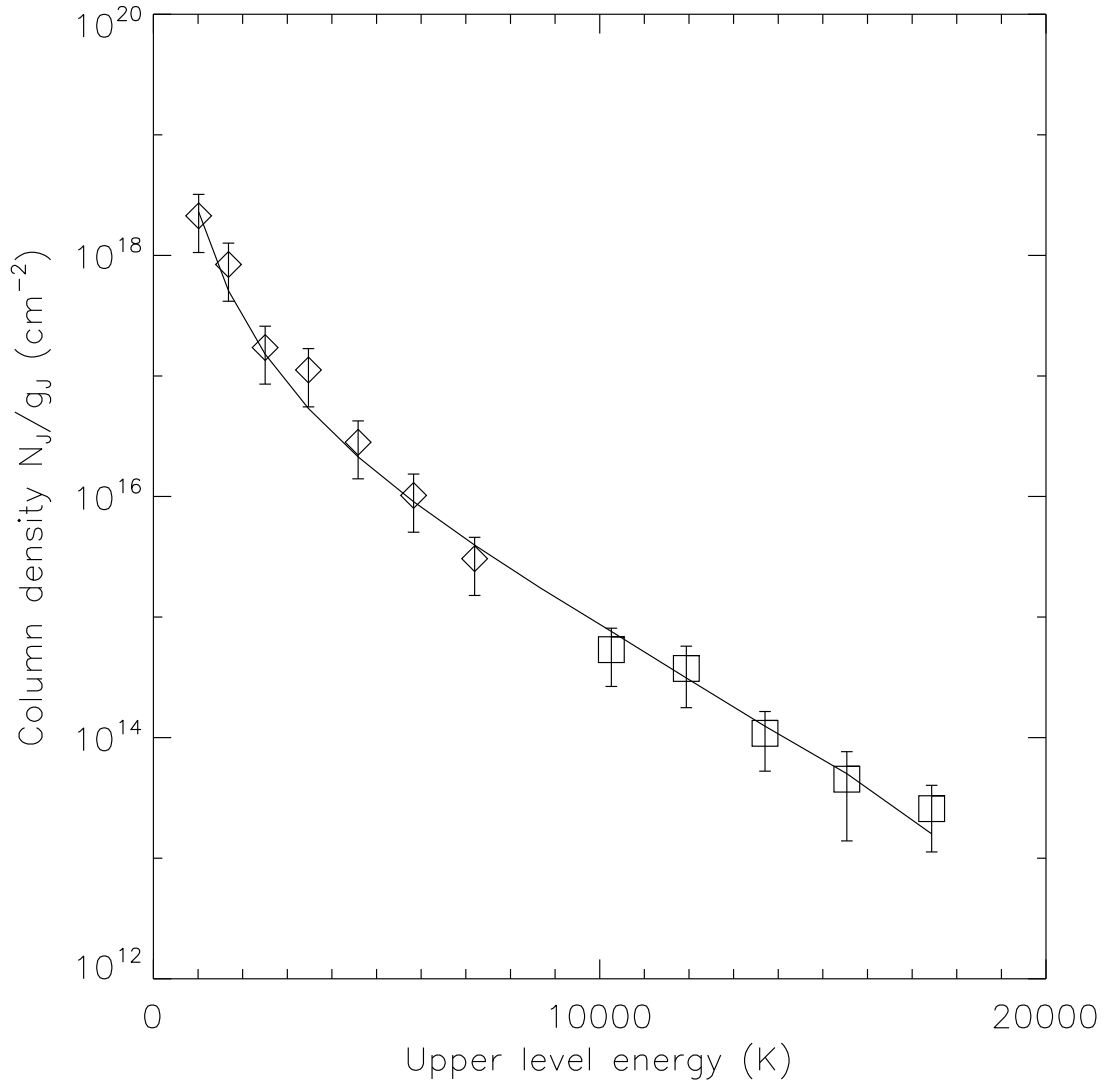


FIG. 6.— Combined *AKARI* (square) and *Spitzer* (diamond) H_2 line population diagram of the western shell. The solid curve represents the prediction of the best-fit parameters of the thermal admixture model.

TABLE 1
SUMMARY OF *AKARI* OBSERVATIONS

Date	ID ^a	Mode	Band
2007. 2. 5.	1400755	IRC imaging	L15, L24
2007. 2. 6.	1400754	FIS imaging	N60, Wide-S, Wide-L, N160
2008. 8. 8.	1420785(1,2), 1420783(1,2), 1421783	IRC spectroscopy	NG
2009. 2. 4.	1420784	IRC spectroscopy	NG
2009. 2. 6.	1421784, 1421785	IRC spectroscopy	NG

^a *AKARI* observational identification number.

TABLE 2
CHARACTERISTICS OF THE IMAGING BANDS.^a

Band	<i>Spitzer</i> 4.5 μm	<i>Spitzer</i> 8 μm	<i>AKARI</i> 15 μm	<i>Spitzer</i> 24 μm	<i>AKARI</i> 24 μm	<i>AKARI</i> 65 μm	<i>AKARI</i> 90 μm	<i>AKARI</i> 140 μm	<i>AKARI</i> 160 μm
Instrument	IRAC 4.5	IRAC 8	IRC L15	MIPS 24	IRC L24	FIS N60	FIS Wide-S	FIS Wide-L	FIS N160
Reference wavelength (μm)	4.49	7.87	15.0	23.68	24.0	65	90	140	160
Effective bandwidth (μm)	1.01	2.93	5.98	5.3	5.34	21.7	37.9	52.4	34.1
FWHM ($''$)	1.72	1.98	5.7	6	6.8	37	39	58	61

^a Detailed characteristics of *AKARI* IRC, *AKARI* FIS *Spitzer* IRAC, and *Spitzer* MIPS are described in Onaka et al. (2007), Kawada et al. (2007), Fazio et al. (2004), and Rieke et al. (2004), respectively.

TABLE 3
SLIT POSITIONS OF *AKARI* SPECTROSCOPIC OBSERVATIONS.

Slit	Position ^a	Exposure
A	(13 ^h 05 ^m 48 ^s , $-62^{\circ}38'39''$)	1 \times 308 s
B1	(13 ^h 05 ^m 33 ^s , $-62^{\circ}40'00''$)	2 \times 308 s
B2	(13 ^h 05 ^m 33 ^s , $-62^{\circ}40'19''$)	1 \times 308 s
C1	(13 ^h 05 ^m 32 ^s , $-62^{\circ}42'34''$)	1 \times 308 s
C2	(13 ^h 05 ^m 33 ^s , $-62^{\circ}42'16''$)	1 \times 308 s
Background ^b	(13 ^h 05 ^m 20 ^s , $-62^{\circ}39'11''$)	1 \times 308 s

^a The slit position angles were fixed to be 127° by the satellite orbit.

^b One of the accompanying $3'' \times 1.0'$ slit data was used for the background spectrum.

TABLE 4
FLUX OF THE WESTERN AND SOUTHERN SHELLS.

Band	Flux ^a	Western shell Line contribution ^b	Southern shell Flux ^a
<i>AKARI</i> 15 μm	2.6 ± 0.5 Jy	75 ± 21 %	1.2 ± 0.2 Jy
<i>Spitzer</i> 24 μm	2.2 ± 0.4 Jy	38 ± 10 %	1.5 ± 0.2 Jy
<i>AKARI</i> 24 μm	3.1 ± 0.7 Jy	39 ± 11 %	1.0 ± 0.3 Jy
<i>AKARI</i> 65 μm	75 ± 15 Jy	16 ± 8 %	<4 Jy
<i>AKARI</i> 90 μm	90 ± 27 Jy	3 ± 2 %	<8 Jy
<i>AKARI</i> 140 μm	104 ± 44 Jy	<5 %	<53 Jy
<i>AKARI</i> 160 μm	75 ± 31 Jy	<5 %	<34 Jy

^a Measured total band flux including continuum and line emission.

^b We estimate the line contribution to the observed band flux using the *Spitzer* IRS and MIPS SED spectra

TABLE 5
SURFACE BRIGHTNESS OF THE OBSERVED H₂ lines.

Line	Wavelength (μm)	A	B1	B2 ($10^{-5} \text{ erg cm}^{-2} \text{ s}^{-1} \text{ sr}^{-1}$)	C1	C2
H ₂ 1-0 O(3)	2.80		11.6 (4.8)	9.7 (4.3)	12.4 (4.7)	2.8 (2.0)
H ₂ 1-0 O(5)	3.24	4.3 (3.1)	10.6 (6.6)	16.4 (4.5)	10.3 (3.1)	5.7 (2.9)
H ₂ 1-0 O(6)	3.50			4.2 (2.0)	7.8 (4.0)	
H ₂ 0-0 S(14)	3.72			2.5 (1.9)	2.9 (1.7)	
H ₂ 1-0 O(7)	3.81		2.6 (1.4)	5.8 (2.2)	6.1 (3.3)	2.2 (2.3)
H ₂ 0-0 S(13)	3.85		6.9 (2.3)	8.4 (2.2)	7.7 (2.4)	3.5 (1.4)
H ₂ 0-0 S(12)	4.00			3.6 (1.7)	1.7 (1.4)	
H ₂ 0-0 S(11)	4.19	7.1 (2.5)	16.0 (2.7)	18.6 (2.3)	17.1 (2.1)	10.7 (2.2)
H ₂ 0-0 S(10)	4.41	8.5 (2.6)	14.0 (2.4)	14.5 (2.5)	15.3 (2.5)	7.8 (2.1)
H ₂ 0-0 S(9)	4.69	13.1 (3.7)	35.1 (1.9)	39.5 (2.9)	37.5 (1.9)	18.5 (1.7)

NOTE. — The numbers in parentheses are measured errors